PET Physics and Instrumentation

8

Srilalan Krishnamoorthy, Jeffrey P. Schmall, and Suleman Surti

Contents

Abstract

The design of instrumentation for positron emission tomography (PET) scanners has vastly progressed over the past ~30 years. In this chapter, we focus on the motivations and technical advancements that lead to the development of multimodality imaging systems, including the integration of PET and CT into combined PET/CT scanners for whole-body imaging. We also provide a review of recent advances in time-of-flight (TOF) PET, ending with a description of current state-of-the-art TOF-PET/CT imaging systems. We begin with

S. Krishnamoorthy, PhD • J.P. Schmall, PhD
S. Surti, PhD (✉)
Department of Radiology, Perelman School of Medicine at the University of Pennsylvania, 156B John Morgan Building, 3620 Hamilton Walk, Philadelphia, PA 19104, USA
e-mail: srilalan@mail.med.upenn.edu; schmall@mail.med.upenn.edu; surti@mail.med.upenn.edu

© Springer International Publishing Switzerland 2017
M.M. Khalil (ed.), *Basic Science of PET Imaging*, DOI 10.1007/978-3-319-40070-9_8

an overview of PET detector design and explore the trade-offs associated with the choice of scintillator, photodetector, and their arrangement. Next, PET data correction approaches, including attenuation correction, for PET/CT are discussed along with a technical description of PET/CT system hardware. Specific concepts and instrumentation aspects of TOF-PET are then reviewed, ending with a brief discussion on the outlook and future directions for PET instrumentation research. This chapter highlights recent advances in PET instrumentation and describes their impact and contribution to the improvement in clinical PET imaging.

8.1 Introduction

The idea for positron annihilation coincidence imaging can be traced to the early days of radionuclide imaging when it was initially explored by Hal Anger [1] and Gordon Brownell [2]. The early instrumentation efforts utilized dual planar stationary detectors that produced longitudinal tomographic images. Subsequently, with the development of transverse section image reconstruction algorithms [3, 4] and the arrival of relatively cost-effective computers in the early to mid-1970s, there was a push toward the development of PET systems providing transverse section images. The system design, therefore, evolved from stationary, dual planar detectors to circular or full angular coverage systems [5–13]. The primary detector design in all these systems utilized scintillation detectors directly coupled to a photomultiplier tube (PMT). Due to PMT sizes, this significantly limited the spatial resolution of these early PET systems. Since then, PET system design has evolved toward higher resolution detectors that are suitable for imaging not only humans but also small animals such as mice.

8.1.1 Positron Annihilation

The signal that is measured in PET originates from unstable neutron-deficient isotopes, which can undergo nuclear decay emitting a positron and a neutrino in the process. The positron has the same mass as an electron but has the opposite charge—it is a form of antimatter that will combine with a free electron resulting in a matter-antimatter annihilation. The probability of positron annihilation and the mean positron energy will vary depending on the specific isotope. The annihilation event transfers the energy mass of the positron, and any residual kinetic energy, to simultaneously create two photons, whose direction is ~180° apart, each having an energy of 511 keV. This may be obvious, but it represents an important distinction: the PET scanner is designed to detect the annihilation photons, not the positron itself, only a signature of its existence. These fundamental characteristics, the simultaneous emission of two, antiparallel, 511 keV photons, form the basis of the detection logic employed by all PET scanners.

8.1.2 Coincidence Logic and Electronic Collimation

Shown in Fig. 8.1 is a schematic of two detectors operating in coincidence mode 180° apart, with a positron source in between them. A coincidence is made when both detectors detect a 511 keV photon at the same time; this tells us that somewhere along a line connecting the two detectors, an annihilation event occurred—we call this coincidence logic. A PET scanner is a scaled-up version of this simple two-detector system, to a full ring of detectors, with each detector able to form coincidences with another detector in the ring. Unlike single-photon emission computed tomography (SPECT), which uses a physical collimator, localization of events in PET is done by electronically collimating events using multiple detector pairs; coincidence combinations within the ring of detectors allow for complete angular and radial sampling of the imaging field of view. Electronic collimation is one of PET's greatest advantages and is a primary reason for PET's high sensitivity. The physical collimation used in SPECT attenuates much of the signal incident on the detector surface; this makes the sensitivity of

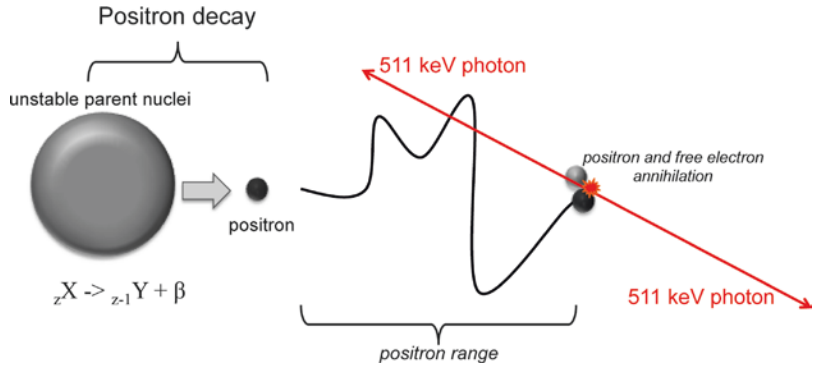

Fig. 8.1 Schematic of positron decay: the unstable parent nuclei decay emitting a positron in the process. The positron travels some distance (referred to as positron range) while losing its kinetic energy through interactions with surrounding molecules before combining with an electron causing an annihilation event to occur. The annihilation results in the emission of two 511 keV photons emitted 180° apart (±0.25°)

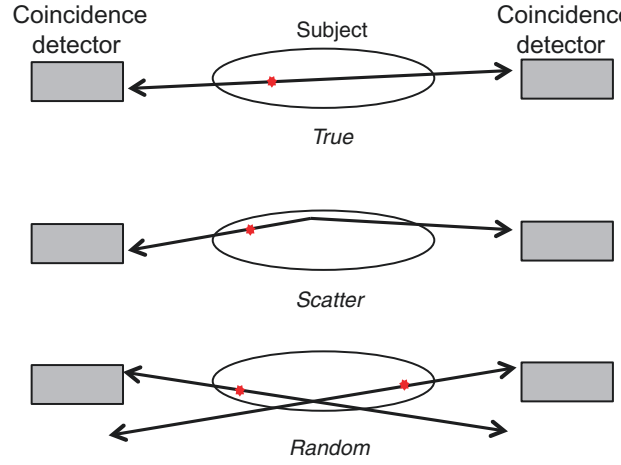

Fig. 8.2 Types of events detected in coincidence. A true event would provide correct localization of the annihilation site; if one or both of the annihilation photons undergo Compton scatter in the tissue and change direction, the event is considered scattered; a random event occurs when two separate decays each contribute a photon to be detected

PET many times higher than SPECT for a comparable midplane resolution.

8.1.3 Types of Events Detected by a PET Scanner

Events from coincidence detection can be categorized into three groups: trues (signal), scatter (background), and randoms (background). Figure 8.2 shows a diagram of a positron source emitting inside of a scattering medium. Ideally, during the detection process, two separate annihilation events would not overlap in time, and photons would not scatter within the body—events meeting these criteria would be considered true events. If either of the two annihilation photons undergoes a Compton scatter interaction before reaching the detector, the event is designated a scattered event. If two decays occur close in time, each contributing at least one photon to be detected, the event is considered a random. Unlike true events, which do not scatter within the body or overlap in time, scatter and random events reduce image quality by adding background signal to the image and reducing contrast.

Because photons lose energy when they scatter and, in theory, there is a very low probability that two events happen at exactly the same time (within ~10^{-12} s), coincidence logic can perfectly distinguish all true events. The detector's ability

to perform coincidence detection is characterized by its energy resolution and timing resolution—parameters that quantify the uncertainty in measuring the photon energy and its time of arrival.

The detector works by creating an electronic pulse when a photon hits the detector. The electronic pulse is then integrated to calculate the total energy deposited. If the detected energy is not 511 keV, the event is typically discarded. Another specialized electronic circuit is used to assign a digital "time stamp" to each detected event. The time stamp is then sent to a coincidence processor, which looks for overlapping coincidences in opposing detectors. If an overlapping time stamp from another detector is found, the event is kept; if no time stamp is found, the event is discarded. A detector with perfect energy resolution and timing resolution would be able to identify all true coincidences and discard any scattered or random events; however, because of the detector's finite resolution, this is not possible in practice.

8.1.4 Time-of-Flight PET

It is possible to measure additional parameters of the positron decay with coincidence detection when using detectors with extremely good timing resolution. A very accurate measurement of the time difference between interactions occurring in the two detectors allows for time-based information to be used to localize the event, as shown in Fig. 8.3. This technique is referred to as time-of-flight PET. The time difference (Δt), between the arrival times of the two coincidence photons, can be related to the location of the annihilation (Δx), with respect to the midpoint between the two detectors, using Eq. 8.1, where c is the speed of light:

$$\Delta x = \left(\Delta t \times c\right)/2 \tag{8.1}$$

A time difference of zero corresponds to the annihilation occurring at the midpoint. The measurement of Δt will have some uncertainty (determined by the detector timing resolution), limiting the precision of Δx. In theory, with perfect timing resolution, image reconstruction would not be needed as all events could be localized in three dimensions with the timing and spatial information from each coincidence detector. As will be discussed later, current clinical whole-body PET scanners achieve a timing resolution of ~375–600 ps, corresponding to a localization uncertainty of about 5.6–9.0 cm; a timing resolution of ~30 ps would be needed for a direct formation of the image without reconstruction. Over the last 10 years, TOF-PET/CT has vastly improved PET imaging quality and capabilities, with all commercial manufacturers offering a TOF-PET/CT scanner model.

8.2 PET Instrumentation

8.2.1 Scintillation Detectors

As described earlier, a PET scanner is designed to detect antiparallel pairs of 511 keV photons originating from positron annihilations and typically consists of a ring of detectors surrounding the imaging subject. The typical role of a detector is to measure the position and energy of the incoming 511 keV photon. Since PET relies on detecting 511 keV photons that occur near in time, PET detectors also need to measure arrival times of the two coincident photons.

The standard PET detector utilizes an inorganic scintillation crystal coupled to a photosensor. The scintillation crystal converts the energy of the ionizing radiation into optical photons that are subsequently detected by the photosensor and converted into an electrical signal. The 511 keV photons interact within the scintillator primarily via photoelectric or Compton interactions and generate electron-hole pairs that transfer this energy to luminescent centers in the scintillator. The process results in the emission of many scintillation (light) photons within a very short time frame (<1 μs). Birks [14] provides a more detailed explanation of this process. An important property of the scintillator is its ability to respond proportionally to the energy deposited by the 511 keV photon, i.e., the number of scintillation photons produced is directly proportional to the

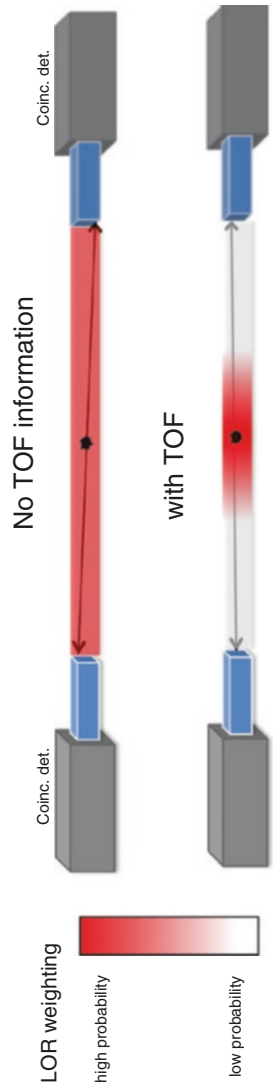

Fig. 8.3 The time-of-flight (*TOF*) information measured through the recorded time difference between the two detectors is incorporated into the image reconstruction model, limiting the event localization probability along the line of response (*LOR*). Without TOF there is a uniform probability applied along the LOR

energy deposited by the 511 keV photon. An ideal PET scintillator should have (i) high density and large atomic number to efficiently stop 511 keV photons with the least amount of scintillator material, (ii) the scintillation light pulse should have fast response to provide high count-rate capability and good timing resolution for rejecting random coincidences, and (iii) high light output and good energy resolution to identify the scattered photons. In addition, the scintillation material should be optically transparent, mechanically rugged, nonhygroscopic, affordable, and easy to produce. While the search for an ideal scintillator is still ongoing [15], amongst currently available scintillators, lutetium-based scintillators such as LSO and LYSO are widely used as they have the best overall characteristics. Their high density (7.1 g/cm^3), high light output (32,000 photons/MeV), and fast response time (decay time = 41 ns) make them appropriate for use in PET [16].

8.2.2 Photosensors

Photomultiplier tubes (PMTs) are the most common photosensor used in scintillation PET detector designs. The PMT is used to convert the scintillation photons into a proportional electrical signal. PMTs are vacuum devices and offer excellent signal-to-noise characteristics for detecting optical photons from scintillators. They are fast, linear, stable, mature, low-noise devices having very high gain (10^6–10^7). While single-channel PMTs have been the standard photosensor used in clinical PET scanners for a long time, these PMTs do not easily permit design of a high spatial resolution detector required for small animal PET. In this scenario, multi-anode (MA) or position-sensitive (PS) PMTs and avalanche photodiodes (APD) provide viable alternatives. In a MA-PMT, a single PMT is segmented into multiple smaller channels with independent anode readout for each channel (N channels along each direction leading to a total of N^2 channels). To decrease the complexity and cost associated with reading out all individual channels of a MA-PMT, a charge-resistive readout network integrated with the PMT anode outputs is sometimes used to encode the interaction position with fewer electronic channels. On the other hand, PS-PMTs utilize a 2D arrangement of cross wired anodes to readout and decode the gamma-ray interaction location. While the MA-PMT has 'N × N' readout channels, the PS-PMT only has 'N + N' readout channels. Unlike PMTs, APDs are solid-state photosensors that are compact, have high quantum efficiency, offer low gamma attenuation, and are insensitive to magnetic fields. APDs are particularly interesting, as they can be made very small and close packed, opening up the possibility of one-to-one coupling of crystal to photosensor that may be needed for developing higher spatial resolution PET detectors.

8.2.3 PET Detector Designs

The first SPECT camera designed by Hal Anger comprised of a single continuous scintillator slab viewed by an array of PMTs and position decoding performed by using a weighted centroid algorithm [17]. Some of the early large-area PET scanners borrowed the same design, albeit with a more appropriate thicker scintillator for PET (Fig. 8.4a). This design is more practical in comparison with the first PET scanners that used a one-to-one coupling scheme with a single PMT to read out a single scintillation crystal [18, 19]. Since then the major detector designs used for clinical PET have relied on using some form of light sharing to decode the gamma-ray interaction location. One approach modifies the original Anger detector to read out an array of pixelated scintillators [20] (Fig. 8.4b). The "block detector" developed in the mid-1980s [21] is another popular design that relies on coupling a scintillator block to four PMTs. Cuts are introduced in the scintillator, and the block is segmented in a careful manner to induce sharing of light between the four PMTs (Fig. 8.4c). A modified version of the block detector concept which uses larger PMTs that overlap adjoining block detectors is known as the quadrant-sharing detector [22]. Higher

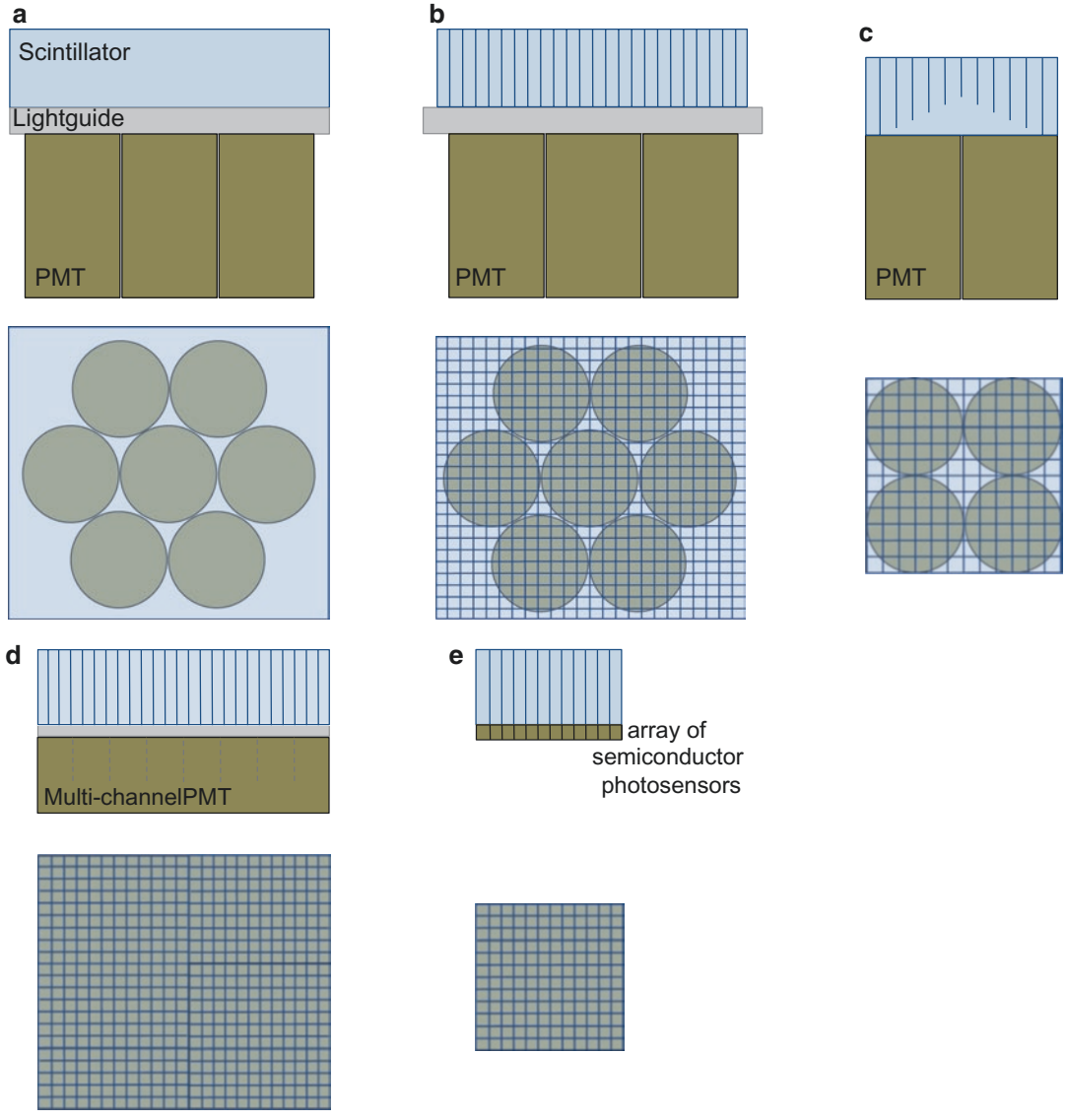

Fig 8.4 Illustration of commonly used PET detector designs used in clinical and preclinical PET scanner designs: (**a**) continuous crystal light-sharing detector, (**b**) pixelated light-sharing detector, (**c**) block detector, (**d**) pixelated light-sharing detector with a multi-anode or position-sensitive PMT, and (**e**) one-to-one coupling detector with an array of solid-state photosensors

spatial resolution detectors required for small animal PET, on the other hand, typically utilize multi-anode or position-sensitive PMTs and APDs in a light-sharing (Fig. 8.4d) or one-to-one coupling design (Fig. 8.4e) configuration [23–29]. Each of the above detector designs has their own merits and trade-offs, but they all provide a practical technique for designing a clinical scanner. Continuous crystal detectors have lower manufacturing costs and offer continuous position sampling, but have limited count-rate capability. The one-to-one or direct coupling detector offers the best count-rate performance but requires a larger number of photosensors and readout electronics, which can increase the scanner complexity and cost. Pixelated light-sharing detectors offer a compromise between count-rate performance and cost. Current

whole-body PET/CT scanners typically use pixelated detectors with 4 mm wide crystals, while small animal scanners use 1.5–2 mm wide crystals.

8.2.4 PET Data Acquisition and Signal Processing

The electrical pulse produced by the PET detector undergoes signal conditioning and processing before being handled by the data acquisition system. The PMT outputs are routed to an amplifier and shaper first, before being digitized by an analog to digital convertor (ADC). Since the timing resolution is very sensitive to the scintillation pulse rise time, separate energy (slow) and timing (fast) pathways are typically employed. A sum of all PMT signals belonging to the full or some predetermined portion of the detector is used to determine event energy and time of arrival, while a weighted centroid algorithm is used to compute the interaction position of the 511 keV photon. The calculated interaction position is mapped to scanner coordinates via a pre-computed look-up table that is generated in a separate scanner calibration step. To efficiently use data acquisition transfer rates and decrease scanner dead time, coincidence detection is followed by energy thresholding (via analog or digital energy discriminators). Only coincidences depositing a predefined minimum energy (typically 300–400 keV) are handled. The position, energy, and TOF information for all valid events are stored by the data acquisition and are used later for performing data corrections and PET image generation.

8.2.5 PET System Design and Geometry

While some of the early generation PET systems made use of flat-panel detectors that were rotated around the patient to collect full tomographic data, these designs eventually evolved to using a stationary ring of detectors. Current whole-body PET scanners have an ~90 cm ring diameter and 16–22 cm axial field of view (FOV). All scanners operate in fully 3D mode and require good energy resolution to discard the scattered radiation and fast scintillators to keep up with the expected count rate in these systems. Lutetium-based scintillators like LSO/LYSO are thus attractive and preferred in current PET/CT scanners.

8.3 PET System Characteristics

8.3.1 Sensitivity

PET scanner sensitivity is defined as the fraction of positron annihilation events that are detected in the scanner. The PET scanner is essentially a photon counter, and the statistical noise is inversely proportional to the square root of the number of coincident events it detects. Hence, scanner sensitivity plays an important role in determining image noise or activity concentrations at which imaging can be performed. A high sensitivity scanner would reduce imaging time and/or permit imaging at lower activity concentration, thereby decreasing the injected activity and/or radiation dose. It would also permit dynamic scans with short-lived isotopes and repeated longitudinal studies without exaggerating concerns over administered dose. Scanner sensitivity is determined by two factors: scanner geometric coverage, also referred to as solid angle, and the scintillator stopping power and thickness. Clinical whole-body scanners use 20–30 mm long crystals with ~20 % angular coverage and typically have ~5–6 % sensitivity for a point source at the center. Small animal scanners use 10–15 mm long crystals with ~40 % scanner angular coverage and achieve typical sensitivity values in the range of ~2–7 % for a point source at the center.

8.3.2 Spatial Resolution

Spatial resolution determines the smallest structure that can be clearly visualized, and a scanner with the highest spatial resolution is necessary to resolve the finest details in an object. Two physic processes that arise from positron decay limit

spatial resolution in PET scanners: positron range and annihilation photon acollinearity. The positron emitted by the radionuclide has some kinetic energy and therefore travels a short distance from the emission point before annihilating with an electron. This positron range is related to its kinetic energy; for ^{18}F (maximum positron energy = 0.635 MeV), the root mean square value of distanced traveled in water is 0.2 mm, while for ^{82}Rb (maximum positron energy = 3.4 MeV), it is 2.6 mm [30, 31]. Annihilation photon acollinearity arises from the conservation of momentum during the electron-positron annihilation process. Instead of being emitted at exactly 180°, there is a small deviation of ±0.25° on account of some residual kinetic energy the positron-electron pair possesses at the time of annihilation. While the deviation is small, its contribution to the spatial resolution degradation is dependent on the scanner diameter, i.e., the larger the diameter of the scanner, the larger its contribution. For whole-body PET scanners having a diameter of 90 cm, the degradation is ~2 mm, while for small animal scanners with an 18 cm ring diameter, the contribution is ~0.4 mm. In addition to the limits from fundamental positron decay physics, PET scanner spatial resolution is also dependent upon the spatial resolution of the detector. The spatial resolution in pixelated-detector designs is limited by the cross section (width) of the individual crystals used in the PET detector. While a theoretical spatial resolution of half the crystal width can be achieved (for events at the center of the scanner), the finite detector sampling over the FOV often degrades it [32]. There are additional contributions from Compton scattering of the 511 keV photon in the detector and the error in interaction position determination due to the use of light-sharing techniques in the detector. Currently clinical PET scanners for whole-body imaging have a spatial resolution in the range of 4–6 mm [33–35], while small animal scanners have a spatial resolution of 1.5–2 mm [36], both of which are primarily determined by the scintillation crystal widths used in the detector.

An additional source of spatial resolution degradation is from parallax error. Events that occur away from the center of the scanner result in the 511 keV photons no longer traveling perpendicular to the scintillator entrance face. Depending on the scintillator depth at which the 511 keV photon interacts, there is an error in determining the correct line of response (LOR). This LOR mispositioning error is known as parallax error (Fig. 8.5) and degrades the overall spatial resolution as a function of the distance from the center of the scanner. Parallax error is particularly evident in small animal scanners since they make use of small ring diameters and long crystals to improve sensitivity. Clinical whole-body scanners have ~90 cm ring diameter and ~50 cm FOV, making them less susceptible to parallax errors.

8.3.3 Energy Resolution

Energy resolution determines the accuracy with which the scanner can measure the energy of the 511 keV photon interactions and affects the ability to reject scatter coincidences where at least one of the two 511 keV photons has incident energy <511 keV. Current clinical whole-body PET scanners using LSO/LYSO scintillators have ~12 % energy resolution that allows the use of a high event energy acceptance threshold (up to 440 keV), thereby collecting all true coincidences with a small fraction of scattered coincidences as well. The importance of energy resolution is less significant for small animal PET where object scatter from the animal is small relative to that observed in clinical whole-body imaging.

8.3.4 Coincidence Timing Resolution

Since a PET scanner relies on collecting coincident pairs of 511 keV photons, the coincidence detection mechanism is an essential component of a PET scanner. In addition to measuring the interaction location and energy, the PET detector also measures time of arrival for both the coincident 511 keV photons. The time within which coincidence pairs are identified is called the coincidence timing window (τ). A smaller τ

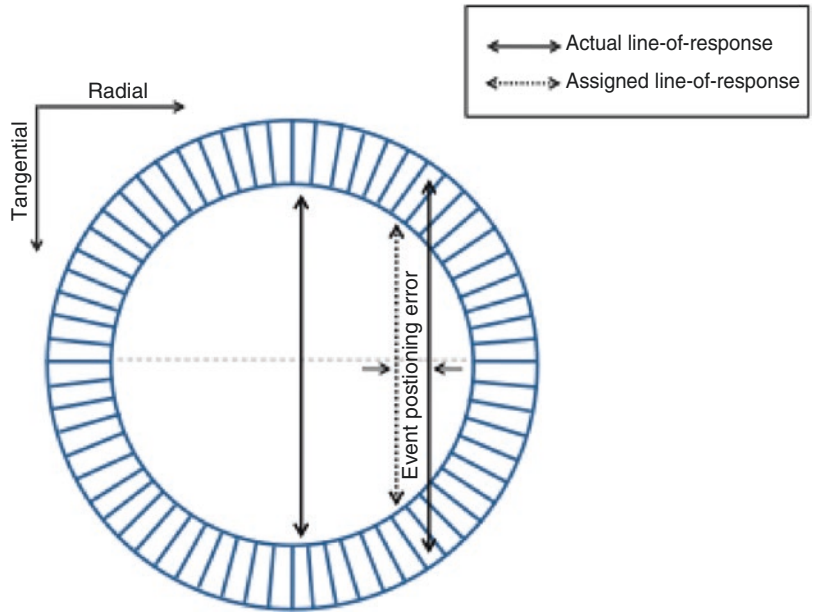

Fig 8.5 Parallax error in a PET scanner: for off-center positron annihilations, there is an error in determining the correct line of response, which degrades the overall spatial resolution of the scanner

will reduce the number of random coincidences collected by the scanner. While the time-of-arrival measurement is fundamentally limited by the timing accuracy of the detector (timing resolution), there is also the path length of the photon to keep in mind. For an annihilation occurring near one detector surface, one of the two 511 keV photon possibly needs to travel much longer before it reaches the detector. In a clinical scanner with ~90 cm ring diameter, it takes the photon ~3 ns to travel this distance. Also, depending on the scanner readout design, either of the two 511 keV photons can be detected first.

8.3.5 Count-Rate Performance

With all scanner designs, there is a minimum amount of time necessary for the scanner to process the event before it is ready to accept another event. This minimum time is referred to as "dead time" and defines the maximum rate at which the scanner can operate. A lower dead-time value (less time in processing events) translates into a higher count-rate capability. While the scanner dead time has contributions from the readout electronics and coincidence processing, it is typically the scintillator conversion process within the detector that primarily limits the overall count-rate performance. A short scintillator signal decay time will allow higher count-rate capability. LSO has an ~40 ns decay time and can provide an average count-rate capability of ~10 million counts/s. Dead time is classified as being either non-paralyzable or paralyzable. A non-paralyzable system will not accept any additional events for processing when it is busy processing an earlier event, and hence all events arriving during this time are simply lost. A paralyzable system on the other hand will process all the events as a single event, increasing the dead time as a result. Dead time arising due to readout electronic limitations is typically non-paralyzable, while scintillator dead time is paralyzable. The count-rate measurement for a scanner is characterized by plotting the measured scanner count rate with a known amount of activity in its FOV. Whatever the mechanism, a scanner with the highest count-rate capability is desirable and remains a priority for PET system designs.

8.4 Multimodality PET/CT

8.4.1 Motivation and Review of Fusion Imaging

Imaging techniques like computed tomography (CT) and magnetic resonance imaging (MRI) offer excellent spatial resolution better than 1 mm and produce exquisite three-dimensional anatomical images. They help in identifying abnormalities based on structural and anatomic changes in the body. While they are well established and are routinely used in the clinic, they provide limited or no physiological information. PET, on the other hand, can measure many different physiological parameters, such as glucose metabolism with ^{18}F-FDG that can help differentiate between malignant and non-malignant tissue. However, the relatively limited spatial resolution of PET makes it difficult to accurately localize such lesions, especially ones that occur in heterogeneous regions like the abdomen or at organ boundaries. To make the best use of their individual strengths, clinicians in the past viewed images acquired from both modalities separately. Differences in the system spatial resolutions, image pixel sizes, and slice thicknesses limited the accuracy with which information from both modalities could be correlated. Several techniques, such as the use of external fiducial markers and stereotactic methods, were developed to correlate the data with other image sets or to an image atlas [37]. Dedicated fusion software that performed co-registration in a semiautomatic or automatic manner was also devised [38–40]. These techniques improved co-registration accuracy, and software fusion found a larger role, especially in brain imaging, as the brain is a sufficiently rigid organ unaffected by organ motion. For whole-body imaging, these techniques were often laborious and sometimes unfeasible. The longer duration for PET imaging meant that whole-body PET images were inconsistent and their resolution affected due to patient breathing. Involuntary internal organ motion and variability/mismatch in patient positioning due to patient transfer and scanner availability constraints added to their troubles. Subsequently, software-based fusion PET/CT found limited success in routine whole-body PET.

8.4.2 Hardware-Based Multimodality PET/CT

The problems encountered by the software-based approach were addressed by a hardware approach to combine them, one that could provide a fully co-registered PET/CT image in a single imaging session. In PET/CT scanners, the PET and CT data are acquired sequentially on a common bed requiring no additional software alignment. While acquiring the two datasets with a single scanner would have been ideal, it engenders several technological challenges that need to be overcome. Apart from improving the scanner readout electronics and count-rate performance, the most important challenge lies in designing a common detector that would work efficiently for both imaging modalities. The very first multimodality nuclear-imaging scanner was designed in the early 1990s and made use of a single high-purity germanium detector to integrate CT with single-photon emission computed tomography (SPECT) [41]. While the prototype scanner demonstrated single detector feasibility, there were some performance compromises, and it was more challenging to adapt for PET/CT. As opposed to the 511 keV photons emitted by PET tracers, the most commonly used SPECT tracer, i.e., Technetium-99 (^{99m}Tc), generates 140 keV photons, close to the X-ray energies used for CT imaging (40–140 keV). The use of a single detector for a PET/CT scanner necessitates compromises for either or both modalities.

It was not until the late 1990s that the first design for a combined PET/CT scanner was presented [42]. It combined an existing partial-ring PET scanner and an existing CT scanner into a single-gantry scanner with a single bed. Independent consoles were used for scanner control, data acquisitions, and image reconstructions. The PET/CT scanner could be operated either independently (i.e., PET or CT) or in a combined

mode with the CT assisting PET imaging. After image reconstruction both the images were sent to a workstation for fused viewing. During normal operation patients were scanned sequentially, first in the CT and then PET. The primary goal of the prototype was to demonstrate the value of a combined scanner providing accurately co-registered PET/CT images. Numerous studies were successfully performed with this prototype that provided sufficient proof of its diagnostic powers and also generated sufficient interest in the clinic [43–47]. Whilst the prototype scanner design was not optimized, it was a significant milestone that spurred the design of next generation PET/CT scanners. Medicare reimbursement approval for certain whole-body FDG-PET scans in 1999 provided further impetus to the utilization and popularity of PET/CT scanners.

By the early 2000s there was enough enthusiasm and clinical evidence for whole-body PET that all major PET vendors began manufacturing and selling PET/CT scanners. Excluding for some variations in the gantry design from each vendor, the commercial PET/CT scanners essentially all include fixed full-ring PET and CT scanners that are melded into a common gantry housing (Fig. 8.6). The individual PET and CT scanners have minimal modifications to potentially offer full performance PET and CT scans, as if they were sold individually. There is typically a gap between the two scanner rings in order to accommodate the scanner readout electronics as well as to minimize the interference (e.g., temperature variations) from each scanner. Care is also taken to match the patient-port sizes for patient comfort. The scanner control and acquisition hardware have better integration than the first prototypes. A common patient couch that traverses the entire axial field of view (FOV) with minimum deflection is key to acquiring accurately co-registered images between the two scanners. Imaging sequences comprise of a short CT scout scan to position the patient within the FOV followed by the CT scan. At the end of the CT scan, the patient couch is translated to the PET FOV and PET imaging begins. Image reconstruction occurs on separate hardware for the PET and CT, each of which is optimized for fast image reconstruction. Proprietary dedicated software to visualize the PET and CT images as overlaid [49–52] or separate images, image analysis, and measurement tools are also provided with the scanner. Figure 8.7 shows an example image acquired with a clinical whole-body PET/CT scanner. As can be seen, the fused PET/CT image improves anatomic localization of lesion within the body.

8.4.3 Attenuation Correction

In PET, the 511 keV photon can interact within the patient and get absorbed or scattered. The linear attenuation coefficient defines this probability of interaction per unit length and is material and photon energy dependent. It increases with the density of the material and decreases with the photon energy. The attenuation probabilities for 511 keV photons is not only dependent on material but also on the object size, i.e., a larger-sized object presents a higher probability of interaction, and the probability is higher for single events near the center than toward its periphery. Attenuation estimation in PET is simplified by the fact that it relies on the detection of both the 511 keV photons that are emitted antiparallel. Let us consider a positron annihilation occurring at depth x in an object with diameter D and linear attenuation μ at 511 keV. The probability (P) that both photons reach the detector is given by the product of their individual transmission probabilities:

$$P = e^{-\mu x} e^{-\mu(D-x)} = e^{-\mu D} \tag{8.2}$$

Thus the total probability is independent of the emission location and only depends on the total path length. The attenuation coefficients for a single LOR can be measured by simply collecting data along that LOR from a known external source placed around the patient. If uncorrected for, attenuation effects produce a nonuniform representation of the true activity distribution, typically observed by a reduced activity in the center of large objects. It can also impair lesion detectability, particularly in heavier patients, as shown in Fig. 8.8.

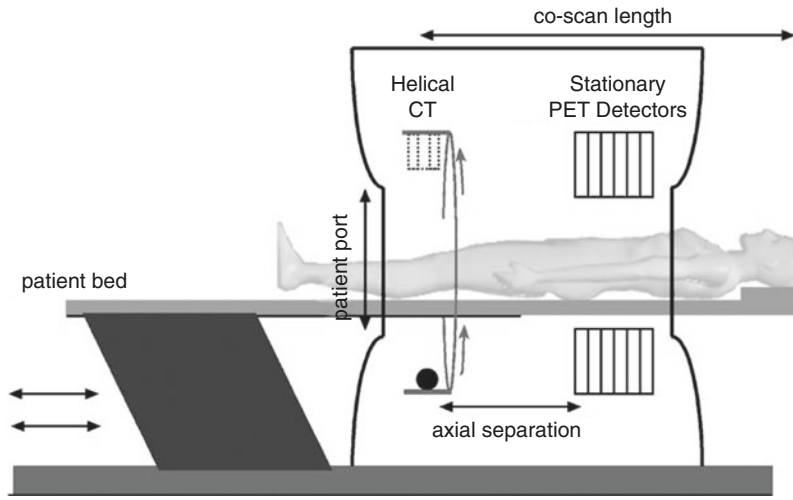

Fig. 8.6 Illustration of current commercial PET/CT scanner designs (Figure reprinted with permission from Alessio et al. [48])

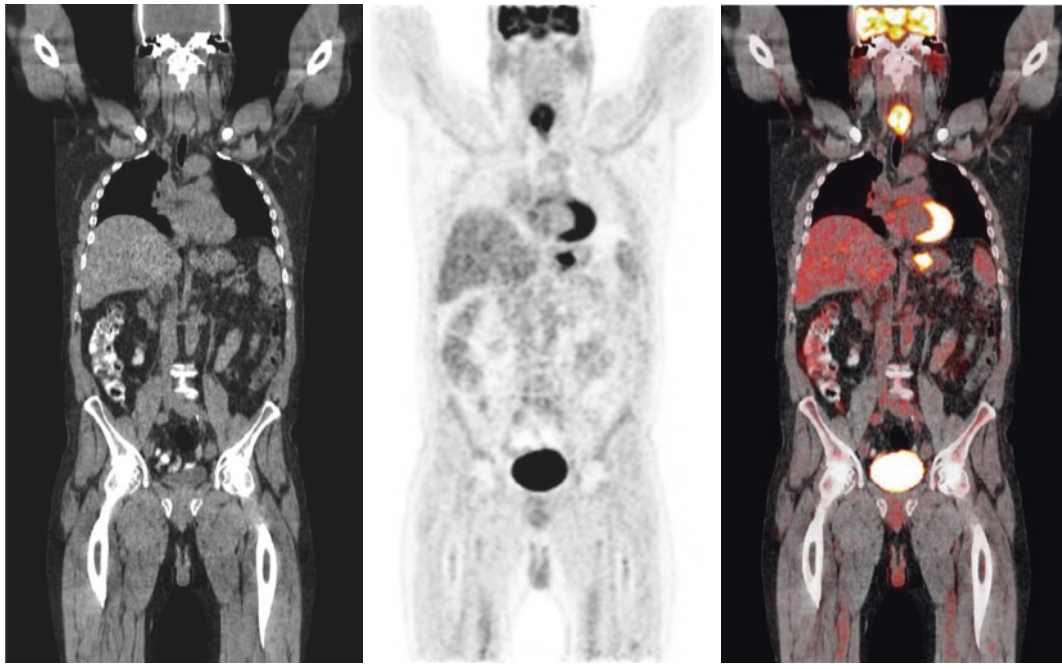

Fig. 8.7 Clinical ^{18}FDG scan images from a whole-body PET/CT scanner. Shown are CT (*left*), PET (*middle*), and fused PET/CT (*right*) images

One of the many advantages offered by multimodality CT is its use for attenuation correction in nuclear-emission imaging. Hasegawa et al. were the first to demonstrate this with their prototype SPECT/CT scanner [41], wherein two separate energy windows were used to collect emission and transmission data simultaneously without interference. The ability to measure attenuation of PET data via CT has even greater significance. Prior to the arrival of PET/CT, PET attenuation was measured by making use of transmission-based methods. A separate

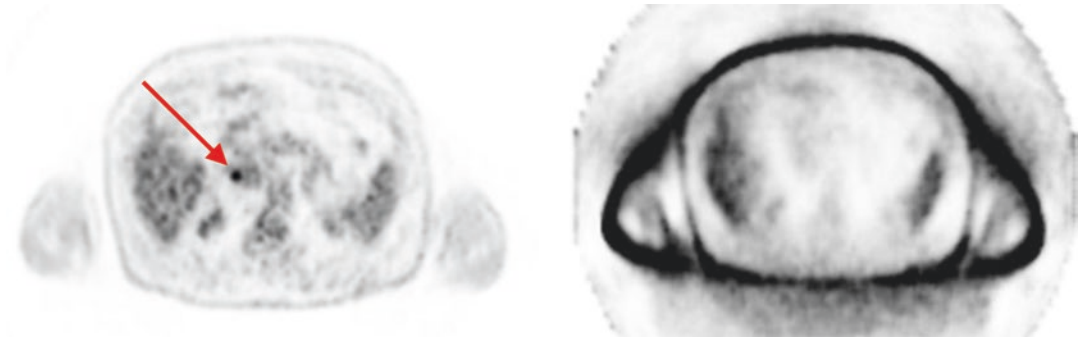

Fig. 8.8 Importance of attenuation correction in PET: Shown are transverse images from a whole-body ^{18}FDG PET scan, with attenuation correction (*left*) and without attenuation correction (*right*). If uncorrected for, attenuation effects can impair lesion detectability (highlighted by the *red arrow*). Images acquired courtesy of the Hospital of the University of Pennsylvania PET Center

transmission scan was measured with a rotating positron or gamma source with the patient laying in the FOV [53, 54]. While each of those techniques had their own merits, the use of a rotating positron source generated the most accurate attenuation map but also introduced statistical noise (on account of counting statistics) into the image reconstruction process. Further reduction of the noise from attenuation estimation required increasing the overall scan time. The availability of CT provides a fast and virtually noise-free alternative to measure the attenuation map. The main concern regarding the use of CT data for PET attenuation lies in the mismatch of energies used for the two measurements. CT scanners use a range of X-ray energies (40–140 keV), and the attenuation values for PET need to be scaled to energy of 511 keV photons. However, at low energies photoelectric interactions dominate, and the CT-measured attenuation depends on both material density and composition. At 511 keV, Compton interactions dominate, and attenuation is primarily dependent on material density alone. Thus a simple scaling of the measured CT attenuation can introduce bias and should not be used for PET. Several techniques using a linear scale factor [55] and a two-layer segmentation and scaling technique [56, 57] have been devised to demonstrate the accuracy in determining attenuation factors from CT [58, 59]. Today, PET/CT scanners are no longer equipped with a rotating source for transmission scanning, and the use of CT for attenuation correction is a standard practice routinely used in clinical PET.

8.4.4 Scatter Correction

The primary mode of interaction for 511 keV photons in the patient is Compton scatter. Compton scattering not only changes the energy of the photon but also alters its direction. The energy and direction of the scattered photon are described by the following equation:

$$E' = \frac{E_\gamma}{1 + \frac{E_\gamma}{m_0 c^2}\left(1 - \cos\theta\right)} \tag{8.3}$$

where E_γ and E' are the energies of the incident (511 keV) and scattered photon, respectively, θ is the scattering angle, and m_0c^2 is the rest mass energy of the electron (511 keV). One or both of the coincident 511 keV photons can undergo single or multiple scattering. If uncorrected, the scattered photons add a background signal to the true activity distribution, lowering image contrast and affecting image quantitation capabilities. Scatter correction techniques can be broadly classified under tail fitting, convolution subtraction, energy based, Monte Carlo, and analytical methods [54]. Amongst them, Monte Carlo-based

simulations provide the most accurate estimate but are also very computationally intensive and impractical to implement on a clinical scanner. The most popular and clinically feasible is a model-based technique called the "single scatter simulation" (SSS) [60–64]. The algorithm assumes single scatter (only one of the two coincident photon scatters and it scatters once) to be the most dominant source of degradation and is a reasonable assumption given the improved energy resolution of current PET scanners allowing higher energy threshold (≥400 keV). In this technique, the initial emission activity distribution is based on the uncorrected emission image, and scatter points are distributed within the measured (i.e., patient specific) attenuation image. For each of the scatter points, the Klein-Nishina equation [65] is used to compute its scatter contribution to each of the LORs in the scanner. The scatter estimate for each LOR is a summation of the computed scatter estimate from all scatter points. The absolute scatter distribution is typically derived by using the tails of the emission data to scale the above estimated scatter distribution. Since the initial emission image will be a poor approximation of the actual activity distribution (uncorrected for scatter), this process is repeated iteratively until a stable scatter distribution is achieved.

8.4.5 Randoms Correction

As described earlier, a random coincidence event is an event wherein two uncorrelated photons arrive within the coincidence time interval (τ). The randoms rate (R) in a scanner can be described by

$$R = 2\tau S_1 S_2 \tag{8.4}$$

where S_1 and S_2 are the single-photon count rates in the two coincident detectors. Randoms correction can be performed based on the single-photon count-rate information (Eq. 8.4) along each LOR. This method called the "singles-based" estimation however requires an accurate knowledge of scanner dead time and detector count rates along each LOR. An alternate technique that is more commonly used for correction of randoms is called the "delayed window technique." In addition to looking for coincidences using the normal coincidence window (τ), it also looks for coincidences using a window that is significantly delayed with respect to the normal coincidence window. Since random coincidences are formed due to random temporal correlation, there should be no true coincidences in the delayed coincidence window (τ_d). While the technique is accurate and simpler for real-time implementation on a scanner, the relatively fewer number of counts can possibly introduce statistical noise in the emission image. Random coincidences are usually stored separately for use during the reconstruction process [54].

8.4.6 Limitations and Issues with PET/CT Imaging

While the improved anatomical localization of lesions, confidence in interpreting scans, and increased clinical throughput have played a significant role in making PET/CT routine, it also has its share of challenges which require attention. Patient movement during the CT scan or in between the CT and PET scans can lead to attenuation correction mismatch and cause artifacts in the PET image. Differences in the respiratory breathing patterns for CT (fast scan performed typically with breath-hold) and PET (longer scan) another area of concern. The use of contrast agents (Fig. 8.9), presence of metallic implants (Fig. 8.10), and areas with significant calcification can generate incorrect attenuation correction factors if not taken into consideration. CT truncation artifacts caused by mismatch between the CT and PET FOV and bias in the CT image caused by beam-hardening effects can also affect the PET data.

8.4.7 Low-Dose CT

Since the dawn of PET/CT, the focus has always been on improving PET scanner performance. With advances in PET detector technology and

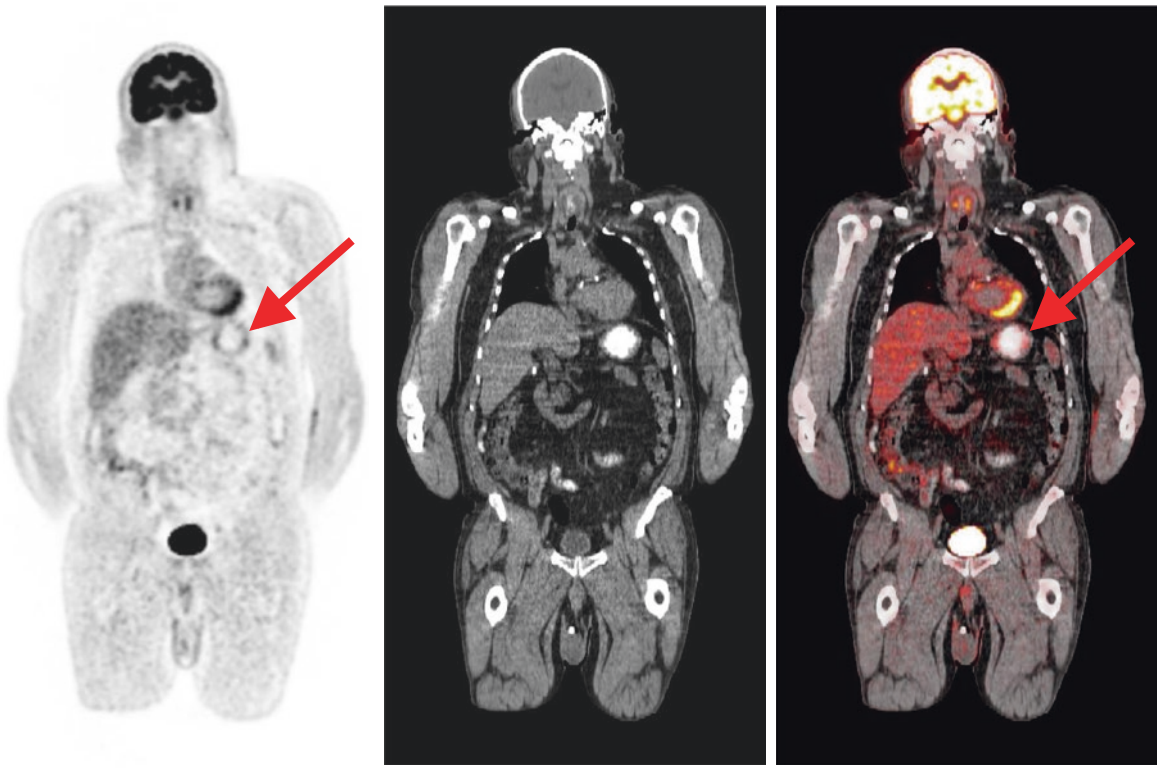

Fig. 8.9 PET artifacts from the use of CT contrast agents in PET/CT: incorrect identification of regions with CT contrast can result in erroneous attenuation correction factors that can affect the PET image. Shown are PET (*left*), CT (*middle*), and fused PET/CT (*right*) images correlating area of CT contrast uptake with radioactivity overestimation (*red arrow*) resulting from IV contrast use. Images acquired courtesy of the Hospital of the University of Pennsylvania PET Center

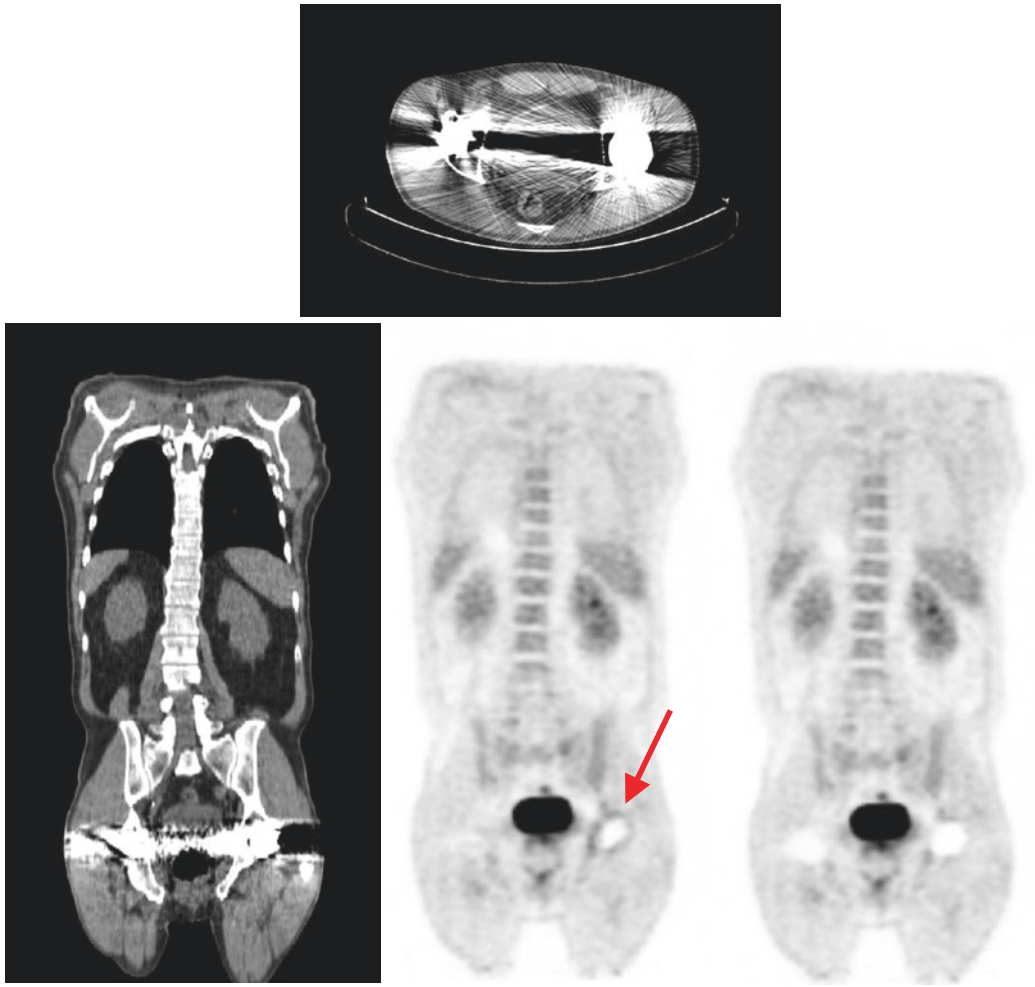

Fig. 8.10 Presence of metallic implants can generate streaking artifacts in CT images, as shown in the transverse (*top*) and coronal (*bottom row left*) CT images from a patient with a hip implant. These artifacts can lead to incorrect estimation of patient attenuation correction factors, and unless corrected for (*bottom row right*), it can lead to incorrect estimation of radioactivity distribution (highlighted by *red arrow* in *bottom row middle*) in the PET image. Images acquired courtesy of the Hospital of the University of Pennsylvania PET Center

scanner design, scan times and image quality have improved significantly. The popularity and effectiveness of PET/CT has led to it being widely used, especially in oncology. The popularity, coupled with the emergence of other multimodality PET devices, has raised concern about the cancer risks associated from receiving additional radiation exposure from CT. The PET improvements have been accompanied by hardware and software improvements in CT that not only improve image quality but also aim to reduce patient dose. Features such as tube current modulation, automatic exposure control, and adaptive collimation lower dose and are now available on many scanners [66–69]. Iterative reconstruction that was impractical previously is now feasible and sufficiently lowers dose without affecting image quality. A full diagnostic CT delivers significantly more dose than one acquired for only assisting the PET. Not only are clinicians making a careful choice here but scanner vendors are also proactively providing options. While the additional dose from CT cannot be completely eliminated, studies have demonstrated that a

task-based optimization of imaging parameters can greatly reduce dose without affecting the clinical outcome [70–73].

8.5 Time-of-Flight PET

8.5.1 Simplified Mathematical Approach to SNR Improvement with Time of Flight

The resurgence of TOF-PET imaging, with the current generation of lutetium-based scanner designs, has provided one of the greatest leaps forward in PET imaging capability and image quality to date. The idea of using TOF information in the reconstruction has been around since the very early days of PET. However, TOF detector designs at the time proved to have a large design trade-off in system performance, most notably poor system spatial resolution that was limited by size of the PMT used in the one-to-one coupled detector. Another big issue at the time was the complexity and stability of the system TOF electronics. Both of these factors led to the use of non-TOF, BGO-based scanners that were commercially manufactured from the late 1980s through the early 2000s—though at least one major manufacturer still sells BGO-based PET/CT systems [74]. In the early 1990s, researchers began to investigate new scintillation materials that could provide excellent timing resolution as well as good stopping power. LSO has been the most widely used, but other materials capable of TOF were discovered [75], such as $LaBr_3$ for which a prototype TOF-PET scanner has been constructed [76].

Many studies have now shown that incorporating TOF information into the reconstruction process improves the quality of the PET data. It is perhaps best to conceptualize this improvement by thinking about the back projection and forward projection processes used in tomographic reconstructions. TOF will limit the probability of localization to an area much less than the entire length of the LOR. Overall, this leads to a reduction in image variance as noise will be spread over fewer image voxels, and also by this same assumption, signal will be more tightly confined. Rigorous mathematical approaches to quantifying the improvement in image SNR with TOF have been attempted [77, 78]. However there are limitations in the mathematical definitions used for the source distribution. Ideally one would use source activities and distributions that are typically encountered during clinical imaging, as what we are really interested in is the clinical improvement in TOF-PET imaging. The approximation that is generally accepted to provide the closest correlation with TOF SNR improvement is well described in Budinger [79]. Assuming you have a uniform distribution of activity in a cylinder of diameter D, the image SNR gain near the center is related to the system timing resolution by $\sqrt{\frac{D}{t}}$, where Δt is the system timing resolution. Because of the Poisson count statistics nature of PET data, one can also view this SNR gain by considering that SNR is proportional to the square root of the total number of events, and therefore an increase in SNR^2 is equivalent to an increase in the number of counts (increase in sensitivity). For this reason, the TOF benefit is often referred to as a sensitivity gain and has been used as an approximate measure to motivate reducing total scan times or lowering patient dose by using a lower amount of injected activity.

8.5.2 Instrumentation Advances Leading to the Reemergence of TOF-PET

There have been several important instrumentation advances that led to the resurgence of TOF: the introduction of LSO as a scintillator used in PET, advances in the system electronics, and improvements in PMT technology. The timing resolution of a scintillator depends on the scintillation pulse temporal characteristics and its total light output. Soon after the discovery of LSO, it was realized that its high light output, short decay time, and fast rise time would allow for a timing resolution comparable to BaF_2 (the scintillator used in first-generation TOF-PET scanners), without sacrificing other performance

characteristics, such as sensitivity and spatial resolution, which are critical for PET [80].

By the late 1990s, bench-top measurements from various research groups had shown that coincidence timing resolution on the order of ~400 ps could be achieved with LSO crystals coupled to commonly used single-channel PMTs [81]. During this time, LSO was also being pursued for use in fully 3D PET, and in 2001 the first commercial whole-body PET scanner was introduced. It was shown that LSO has a clear advantage over BGO in fully 3D PET; however, the system achieved a timing resolution of ~3 ns [82]—an improvement over BGO systems but not capable of TOF reconstruction. Though the scintillation light pulse from LSO was capable of resolutions needed for TOF, the system electronics of the PET scanner could not process events to that degree of timing accuracy. Over the next several years (2001–2006), significant upgrades to the PET system electronics were made allowing the full benefit of LSO timing properties to be used [33]. New PMT technology was also implemented into the later TOF scanner designs, which focused on improved timing performance of the PMT itself and better quantum efficiency [83]. It is also worth mentioning, that even though the fundamental detector module design did not drastically change, a crystal-by-crystal timing correction was implemented, as well as methods for system timing calibration [84–86].

8.5.3 Benefits of TOF Information for Clinical PET Imaging

It is perhaps most straightforward to quantify the TOF benefit in phantom studies where the source distributions are simple, having known locations and activity concentrations. Based on results from these experiments, it is obvious that TOF has improved the quality of the data. However, the more important and relevant question is to understand the degree of this improvement in clinical imaging studies—this is a much more difficult problem [87, 88]. No single metric, such as the SNR gain discussed previously, can describe the benefit of TOF-PET in clinical studies; primarily because clinical imaging tasks are different from imaging uniform phantoms, and the use of iterative reconstruction algorithms, which have become standard in clinical imaging, have varying parameter settings and trade-offs that need to be considered.

In clinical use, TOF information independently improves several components of the PET imaging process—from reducing the impact of errors in data correction to improving the detection and quantification of lesions in oncology imaging and lowering patient dose. It has been observed that TOF-PET data, compared to non-TOF-PET data, is much more robust and less sensitive to errors in applied data corrections, such as attenuation, scatter, and normalization [89]. As an example, Fig. 8.11 shows a comparison of TOF vs non-TOF reconstructions with a shifted attenuation correction map. Artifacts are produced in the non-TOF image due to the mismatch between emission data and the attenuation map. However, with TOF information, these incorrect areas of increased or decreased uptake are reduced.

Another important benefit of TOF-PET data for clinical imaging is the improved convergence observed in iterative reconstruction methods. Shown in Fig. 8.12 are contrast recovery coefficients for lesions using reconstruction algorithms with and without TOF information. Though an absolute quantification of the lesion is difficult, and will vary from patient to patient, the improved convergence of the TOF reconstruction generally provides a better trade-off between lesion contrast and noise [87].

Improved lesion contrast and noise trade-off with TOF-PET naturally results in improved oncology imaging where the primary task of PET is to detect and quantify the uptake of cancer lesions [90]. This was demonstrated for clinical studies by Surti et al. [91] using a lesion insertion technique, to create artificial images from clinical patient data mixed with known lesion locations and activities, and human observes to quantify the impact of TOF-PET on whole-body oncologic studies over non-TOF-PET. The methodology was then extended to study the improvement in accuracy and precision of lesion uptake with

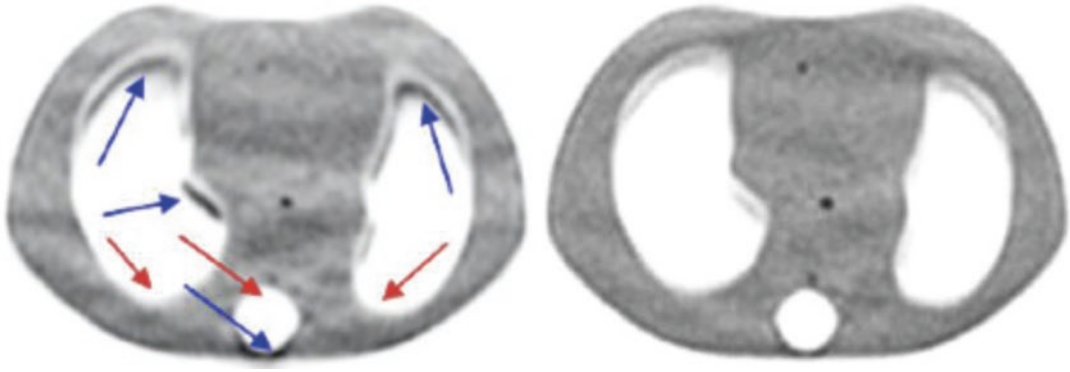

Fig. 8.11 Non-TOF (*left*) and TOF (*right*) images of a thorax phantom using a shifted attenuation correction map. *Arrows* in the non-TOF image indicate incorrect areas of increased and decreased counts (Figure reprinted with permission from [89])

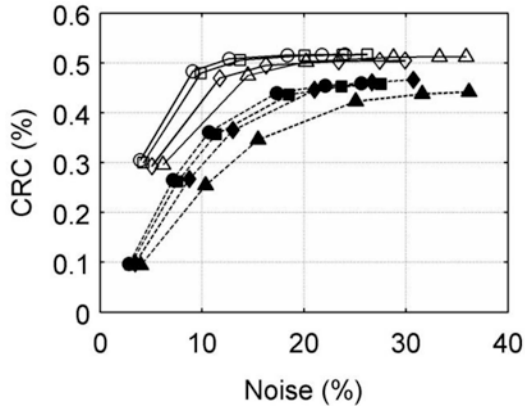

Fig. 8.12 CRC vs noise curves for 17-mm hot spheres with 6:1 contrast in a 35-cm diameter cylinder. Scan times were 2 (σ), 3 (υ), 4 (ν), and 5 (λ) min (35-cm phantom) with closed symbols for non-TOF and open symbols for TOF reconstruction as a function of number of iterations (1, 2, 5, 10, 15, and 20) (Figure reprinted with permission from [87])

TOF-PET [92] and also demonstrated further improvement with better TOF resolution of the scanner.

Another benefit of TOF-PET in clinical imaging is the improvement observed in reconstructed images of larger body mass index (BMI) patients, as shown in Fig. 8.13. This is important because TOF-PET, compared to non-TOF-PET, provides a more uniform clinical performance over a wide range of patient sizes leading to more consistent image quality in all studies. This result is also consistent with the expected SNR gain due to TOF being proportional to $\sqrt{\frac{D}{t}}$.

The TOF gain in larger patients will be higher, and this offsets the effects of increased scatter and attenuation in these patients, which roughly equates to the image quality observed in average size patients.

Lastly, except for benefits in data corrections, the improvement from TOF-PET can generally be replicated by increasing the number of counts used in the reconstruction; without TOF this can only be done by either increasing the scan time or increasing the injected activity—both of these are undesirable in the clinical application of PET. Conversely, while keeping image quality constant, improving TOF will allow for reduced scan times and injected activities leading to a higher patient throughput and lower patient dose. Most clinical imaging protocols using TOF-PET already benefit from lower scan times and resulting in better patient throughput. Further improvement in scanner TOF resolution will yield higher gains in patient throughput. It is anticipated that new generations of TOF-PET scanners with timing resolutions ranging from 350–400 ps will therefore use their improved TOF capability to lower patient dose. In [93], a more detailed summary of the benefits of TOF imaging for clinical imaging is provided.

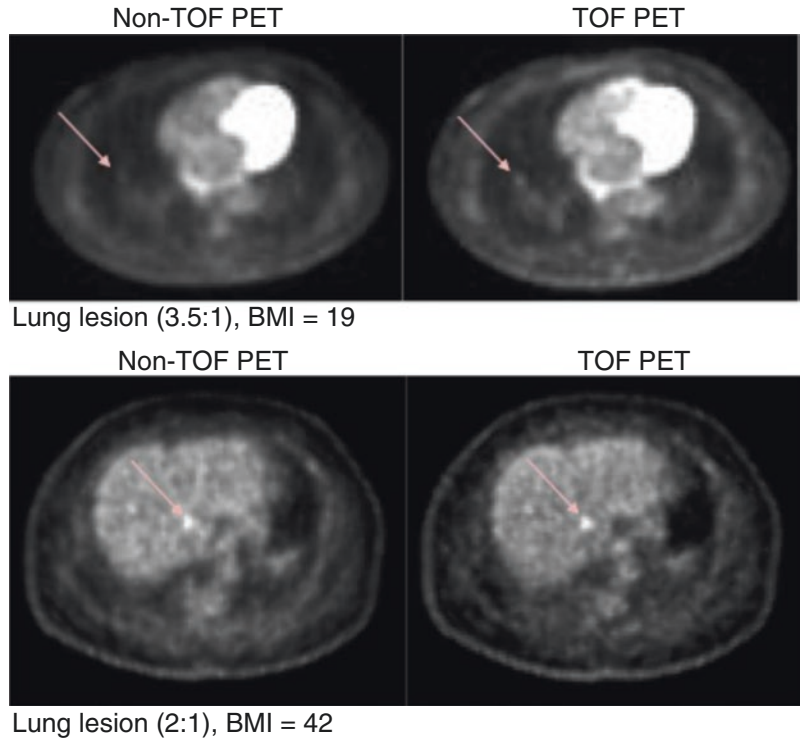

Fig. 8.13 "Lesion present" (*arrow*) transverse slices showing a lung lesion in a subject patient with normal BMI = 19 (*top*) and a liver lesion (*2:1*) in a patient with a BMI = 42 (*bottom*) (Figure reprinted with permission from [90])

8.6 Advances and Future Directions

8.6.1 Silicon Photomultiplier and Its Impact

Basic PET detector design has not changed significantly in more than two decades. However, advances in scintillator, photosensor technology, and data acquisition/electronics design have made clinical PET imaging faster and of higher image quality. While PMT technology continues to improve and is the standard photosensor used in clinical PET, solid-state photosensor technology is also maturing rapidly. An exciting development over the last decade has been the introduction of silicon photomultipliers (SiPMs). SiPMs are solid-state devices that combine the best properties of PMTs and APDs. They are compact, fast, high gain, low noise, and insensitive to magnetic fields [94, 95]. Hence they allow design of fast, high spatial resolution PET detectors that are not only TOF capable but can also operate in high-strength magnetic field. In recent years, a number of research scanners that utilize the advantages of SiPMs in a light-sharing detector design or 1:1 coupling (Fig. 8.4) have been developed [96]. In fact, SiPM-based whole-body PET scanners having system timing resolution of 300–400 ps are already commercially available [97, 98].

8.6.2 Multimodality PET/MR

The complementary information collected from PET and other established imaging modalities such as CT and MRI has always attracted a multimodality approach to combining them. While PET/MR was envisioned before PET/CT, the rapid success of combined PET/CT reinvigorated scientists into looking at ways to combine PET and MRI into a single imaging modality. While a detailed description of the challenges, strategies, and applications of multimodality PET/MR is provided in Chap. 9, it is important to note that

unlike PET/CT, PET/MR was first made available for preclinical use [96]. It was not until the mid-2000s when APD technology matured that it became available, first for dedicated brain imaging [99] and then a few years later for whole-body PET/MR imaging [100]. Due to the noise properties of APDs, these APD-based PET/MR scanners are not TOF capable. However, rapid adoption of SiPM technology has now enabled development of clinical TOF-PET/MR scanners and made them commercially available [98].

8.6.3 Organ-Specific Imaging

Current whole-body PET has a spatial resolution of about 4–6 mm. This is a serious limitation, especially for imaging smaller organs where one often encounters smaller structures and lesions. The use of a dedicated scanner offers several benefits. Due to the size of the organs, the scanner diameter can be reduced. The lower amount of scintillator reduces scanner cost, and the larger geometric coverage increases the scanner sensitivity. While the smaller diameter can cause parallax errors, there is also a decrease in contribution from positron acollinearity. Overall, a dedicated scanner can improve image quality and quantitation by offering higher spatial resolution and sensitivity at lower cost. Dedicated PET scanners were first developed for brain imaging [101–104], but the introduction of dedicated or multimodality PET/MRI [99] has reduced enthusiasm for stand-alone brain PET scanners. Dedicated breast PET however has continued to garner attention with a few research scanners demonstrating better and accurate lesion detection, especially in patients with dense breasts [105].

8.6.4 Direct Conversion Detectors

While scintillators are more efficient in stopping the 511 keV photons, direct gamma-ray conversion detectors making use of cadmium telluride (CdTe) or cadmium zinc telluride (CZT) are now also more widely available. They offer excellent energy resolution (~3 % at 511 keV) and can be highly segmented to offer high (<1 mm) spatial resolution. Although the technology has not been translated for whole-body clinical PET, they appear promising for small animal PET due to the potential for achieving very high and uniform spatial resolution [106–109].

8.7 Summary

PET instrumentation and system design have seen a continuous evolution ever since the first systems were conceived. System spatial resolution has improved by an order of magnitude for clinical imaging. In parallel, system sensitivity has increased with the scanner designs utilizing longer axial coverage and higher-efficiency detectors. Reintroduction of TOF imaging in recent years without any performance trade-offs in terms of system spatial resolution and sensitivity has further transformed the performance of these systems. Combined with a CT scanner, modern TOF-PET/CT produces very high quality and quantitative images in imaging times of <10 min. New technical developments are ongoing that promise further gains not only in PET performance but also opening of new imaging areas.

References

1. Anger HO. Gamma-ray and positron scintillation camera. Nucleonics. 1963;21:10–56.
2. Brownell GL, et al. New developments in positron scintigraphy and the application of cyclotron produced positron emitters In: Medical Radioisotope Scintigraphy; 1969; IAEA (Proceedings Series), Vienna. p. 163–76.
3. Kuhl DE, Edwards RQ. Cylindrical and section radioisotope scanning of the liver and brain. Radiology. 1964;83(5):926–36.
4. Cormack AM. Representation of a function by its line integrals, with some radiological applications. J Appl Phys. 1963;34(9):2722–7.
5. Phelps ME, et al. Design considerations for a positron emission transaxial tomograph (PET III). IEEE Trans Nucl Sci. 1976;23(1):516–22.
6. Cho ZH, Farukhi MR. Bismuth germanate as a potential scintillation detector in positron cameras. J Nucl Med. 1977;18(8):840–4.
7. Terpogossian MM, et al. Design considerations for a positron emission transverse tomograph (pett-V) for

imaging of brain. J Comput Assist Tomogr. 1978; 2(5):539–44.
8. Bohm C, Eriksson L, Bergstrom M, Litton J, Sundman R, Singh M. A computer assisted ring detector positron camera system for reconstruction tomography of the brain. IEEE Trans Nucl Sci. 1978;NS-25:624–37.
9. Thompson CJ, Yamamoto YL, Meyer E. Positome II: a high efficiency positron imaging device for dynamic brain studies. IEEE Trans Nucl Sci. 1979; 26(1):583–9.
10. Derenzo SE, et al. Imaging properties of a positron tomograph with 280-Bgo-crystals. IEEE Trans Nucl Sci. 1981;28(1):81–9.
11. Cho ZH, et al. High-resolution circular ring positron tomograph with dichotomic sampling: Dichotom-I. Phys Med Biol. 1983;28(11):1219–34.
12. Wong WH, et al. Performance characteristics of the University of Texas TOF PET-I camera. J Nucl Med. 1984;25(5):46–7.
13. Burnham CA, Bradshaw J, Kaufman D, Chesler DA, Brownell GL. Positron tomograph employing a one dimension BGO scintillation camera. IEEE Trans Nucl Sci. 1983;30:661–4.
14. Birks JB. The theory and practice of scintillation counting. London: Pergamon Press; 1964.
15. Derenzo SE, et al. The quest for the ideal inorganic scintillator. Nucl Instrum Methods Phys Res Sect A: Accelerators Spectrometers Detectors and Associated Equipment. 2003;505(1-2):111–7.
16. Saint-Gobain Crystals. LYSO/Prelude420 datasheet. 2015. Available from: http://www.crystals.saint-gobain.com/uploadedFiles/SG-Crystals/Documents/PreLude420datasheet.pdf.
17. Anger HO. Scintillation camera. Rev Sci Instrum. 1958;29(1):27–33.
18. Ter-Pogossian MM, et al. A positron-emission transaxial tomograph for nuclear imaging (PETT). Radiology. 1975;114(1):89–98.
19. Hoffman EJ, et al. Design and performance-characteristics of a whole-body positron transaxial tomograph. J Nucl Med. 1976;17(6):493–502.
20. Surti S, et al. Optimizing the performance of a PET detector using discrete GSO crystals on a continuous lightguide. IEEE Trans Nucl Sci. 2000;47:1030–6.
21. Casey ME, Nutt R. A multicrystal two dimensional BGO detector system for positron emission tomography. IEEE Trans Nucl Sci. 1986;33(1):460–3.
22. Wong W-H, et al. A 2-dimensional detector decoding study on BGO arrays with quadrant sharing photomultipliers. IEEE Trans Nucl Sci. 1994;41(4):1453–7.
23. Lightstone AW, et al. A Bismuth Germanate-avalanche photodiode module designed for use in high resolution positron emission tomography. IEEE Trans Nucl Sci. 1986;33(1):456–9.
24. Watanabe M, et al. A high resolution PET for animal studies. IEEE Trans Med Imaging. 1992;11:577–80.
25. Watanabe M, et al. A compact position-sensitive detector for PET. IEEE Trans Nucl Sci. 1995;42(4): 1090–4.
26. Cherry SR, et al. MicroPET: a high resolution PET scanner for imaging small animals. IEEE Trans Nucl Sci. 1997;44:1161–6.
27. Lecomte R, et al. Design and engineering aspects of a high-resolution positron tomograph for small animal imaging. IEEE Trans Nucl Sci. 1994;41(4): 1446–52.
28. Ziegler SI, et al. A prototype high-resolution animal positron tomograph with avalanche photodiode arrays and LSO crystals. Eur J Nucl Med. 2001; 28(2):136–43.
29. Vaska P, et al. RatCAP: miniaturized head-mounted PET for conscious rodent brain imaging. IEEE Trans Nucl Sci. 2004;51(5):2718–22.
30. Derenzo SE. Mathematical removal of positron range blurring in high-resolution tomography. IEEE Trans Nucl Sci. 1986;33(1):565–9.
31. Levin CS, Hoffman EJ. Calculation of positron range and its effect on the fundamental limit of positron emission tomography system spatial resolution. Phys Med Biol. 1999;44(3):781–99.
32. Brooks RA, et al. Sampling requirements and detector motion for positron emission tomography. IEEE Trans Nucl Sci. 1979;NS-26:2760–3.
33. Surti S, et al. Performance of Philips Gemini TF PET/CT scanner with special consideration for its time-of-flight imaging capabilities. J Nucl Med. 2007;48(3):471–80.
34. Bettinardi V, et al. Physical performance of the new hybrid PET/CT discovery-690. Med Phys. 2011;38(10):5394–411.
35. Jakoby BW, et al. Physical and clinical performance of the mCT time-of-flight PET/CT scanner. Phys Med Biol. 2011;56(8):2375–89.
36. Goertzen AL, et al. NEMA NU 4-2008 comparison of preclinical PET imaging systems. J Nucl Med. 2012;53(8):1300–9.
37. Bergstrom M, et al. Determination of object contour from projections for attenuation correction in cranial positron emission tomography. J Comput Assist Tomogr. 1982;6(2):365–72.
38. Hill DL, et al. Medical image registration. Phys Med Biol. 2001;46(3):R1–45.
39. Hutton BF, Braun M. Software for image registration: algorithms, accuracy, efficacy. Semin Nucl Med. 2003;33(3):180–92.
40. Slomka PJ. Software approach to merging molecular with anatomic information. J Nucl Med. 2004;45: 36S–45.
41. Lang TF, et al. Description of a prototype emission-transmission computed tomography imaging system. J Nucl Med. 1992;30(10):1881–7.
42. Beyer T, et al. A combined PET/CT scanner for clinical oncology. J Nucl Med. 2000;41(8):1369–79.
43. Charron M, et al. Image analysis in patients with cancer studied with a combined PET and CT scanner. Clin Nucl Med. 2000;25(11):905–10.
44. Kluetz PG, et al. Combined PET/CT imaging in oncology. Impact on patient management. Clin Positron Imaging. 2000;3(6):223–30.

45. Meltzer CC, et al. Whole-body FDG PET imaging in the abdomen: value of combined PET/CT. J Nucl Med. 2001;42(5):35p.
46. Meltzer CC, et al. Combined FDG PET/CT imaging in head and neck cancer: impact on patient management. J Nucl Med. 2001;42(5):36p.
47. Yeung HW, Schoder H, Larson SM. Utility of PET/CT for assessing equivocal PET lesions in oncology-initial experience. J Nucl Med. 2002;43:32P.
48. Alessio AM, et al. PET/CT scanner instrumentation, challenges, and solutions. In: Alavi A, editor. PET imaging I. Philadelphia: W. B. Saunders Company; 2004. p. 1017–32.
49. Rhem K, et al. Display of merged multimodality brain images using interleaved pixels with independent color scales. J Nucl Med. 1994;35(11):1815–21.
50. Hutton BF, et al. Image registration: an essential tool for nuclear medicine. Eur J Nucl Med. 2002;29(4):559–77.
51. Stokking R, Zubal G, Viergever MA. Display of fused images: methods, interpretation, and diagnostic improvements. Semin Nucl Med. 2003;33(3):219–27.
52. Baum KG, Helguera M, Krol A. Fusion viewer: a new tool for fusion and visualization of multimodal medical data sets. J Digit Imaging. 2008;21(1):59–68.
53. Bailey DL. Transmission scanning in emission tomography. Eur J Nucl Med. 1998;25(7):774–87.
54. Valk PE, et al., editors. Positron emission tomography: basic science and clinical practice. London: Springer; 2003.
55. LaCroix KJ, et al. Investigation of the use of X-ray CT images for attenuation compensation in SPECT. IEEE Trans Nucl Sci. 1994;41(6):2793–9.
56. Kinahan PE, et al. Attenuation correction for a combined 3D PET/CT scanner. Med Phys. 1998;25(10):2046–53.
57. Kinahan PE, Hasegawa BH, Beyer T. X-ray-based attenuation correction for positron emission tomography/computed tomography scanners. Semin Nucl Med. 2003;33(3):166–79.
58. Nakamoto Y, et al. PET/CT: comparison of quantitative tracer uptake between germanium and CT transmission attenuation-corrected images. J Nucl Med. 2002;43(9):1137–43.
59. Burger C, et al. PET attenuation coefficients from CT images: experimental evaluation of the transformation of CT into PET 511-keV attenuation coefficients. Eur J Nucl Med Mol Imaging. 2002;29(7):922–7.
60. Ollinger JM. Model-based scatter correction for fully 3D PET. Phys Med Biol. 1996;41(1):153–76.
61. Watson CC, Newport D, Casey ME. A single scatter simulation technique for scatter correction in 3D PET. Three-Dimens Image Reconstr Radiol Nucl Med. 1996;4:255–68.
62. Accorsi R, et al. Optimization of a fully 3D single scatter simulation algorithm for 3D PET. Phys Med Biol. 2004;49(12):2577–98.
63. Werner ME, Surti S, Karp JS. Implementation and evaluation of a 3D PET single scatter simulation with TOF modeling. In: 2006 IEEE Nuclear Science Symposium and Medical Imaging Conference, San Diego; 2006.
64. Watson CC. Extension of single scatter simulation to scatter correction of time-of-flight PET. IEEE Trans Nucl Sci. 2007;54(5):1679–86.
65. Knoll GF. Radiation detection and measurement. 4th ed. Hoboken: Wiley; 2010.
66. Kalender WA, Wolf H, Suess C. Dose reduction in CT by anatomically adapted tube current modulation. II phantom measurements. Med Phys. 1999;26(11):2248–53.
67. McCollough CH, Bruesewitz MR, Kofler JM. CT dose reduction and dose management tools: overview of available options. Radiographics. 2006;26(2):503–12.
68. Tzedakis A, et al. The effect of z overscanning on patient effective dose from multidetector helical computed tomography examinations. Med Phys. 2008;32(6):1621–9.
69. Deak PD, et al. Effects of adaptive section collimation on patient radiation dose in multisection spiral CT. Radiology. 2009;252(1):140–7.
70. Elstrom RL, et al. Combined PET and low-dose, noncontrast CT scanning obviates the need for additional diagnostic contrast-enhanced CT scans in patients undergoing staging or restaging for lymphoma. Ann Oncol. 2008;19(10):1770–3.
71. Alessio AM, et al. Weight-based, low-dose pediatric whole-body PET/CT protocols. J Nucl Med. 2009;50(10):1570–7.
72. Xia T, et al. Ultra-low dose CT attenuation correction for PET/CT. Phys Med Biol. 2012;2012(57):2.
73. Tonkopi E, Ross AA, MacDonald A. CT dose optimization for whole-body PET/CT examinations. Am J Roentgenol. 2013;201(2):257–63.
74. Lewellen TK, Time-of-flight PET. Semin Nucl Med. 1998;28(3):268–75.
75. Conti M, et al. Comparison of fast scintillators with TOF PET potential. IEEE Trans Nucl Sci. 2009;56(3):926–33.
76. Daube-Witherspoon ME, et al. Imaging performance of a $LaBr_3$-based time-of-flight PET scanner. Phys Med Biol. 2010;55:45–64.
77. Tomitani T. Image reconstruction and noise evaluation in photon time-of-flight assisted positron emission tomography. IEEE Trans Nucl Sci. 1981;28(6):4582–9.
78. Surti S, et al. Investigation of time-of-flight benefit for fully 3-D PET. IEEE Trans Med Imaging. 2006;25(5):529–38.
79. Budinger TF. Time-of-flight positron emission tomography – status relative to conventional PET. J Nucl Med. 1983;24(1):73–6.
80. Moses WW. Time of flight in PET revisited. IEEE Trans Nucl Sci. 2003;50(5):1325–30.
81. Moses WW, Derenzo SE. Prospects for time-of-flight PET using LSO scintillator. IEEE Trans Nucl Sci. 1999;46(3):474–8.

82. Spinks TJ, Bloomfield PM. A comparison of count rate performance for 15O-water blood flow studies in the CTI HR+ and Accel tomographs in 3D mode. In: IEEE Nuclear Science Symposium and Medical Imaging Conference, Norfolk; 2002.
83. Moszynski M, et al. New Photonis XP20D0 photomultiplier for fast timing in nuclear medicine. Nucl Instrum Meth A. 2006;567(1):31–5.
84. Thompson CJ, Camborde M-L, Casey ME. A central positron source to perform the timing alignment of detectors in a PET scanner. IEEE Trans Nucl Sci. 2005;52(5):1300–4.
85. Perkins AE, et al. Time of flight coincidence timing calibration techniques using radioactive sources. In: 2005 IEEE Nuclear Science Symposium and Medical Imaging Conference, San Juan; 2005.
86. Lenox MW, et al. Digital time alignment of high resolution PET Inveon block detectors. In: IEEE Nuclear Science Symposium and Medical Imaging Conference, San Diego; 2006.
87. Karp JS, et al. Benefit of time-of-flight in PET: experimental and clinical results. J Nucl Med. 2008;49(3):462–70.
88. Lois C, et al. An assessment of the impact of incorporating time-of-flight information into clinical PET/CT imaging. J Nucl Med. 2010;51:237–45.
89. Conti M. Why is TOF PET reconstruction a more robust method in the presence of inconsistent data? Phys Med Biol. 2011;56:155–68.
90. El Fakhri G, et al. Improvement in lesion detection with whole-body oncologic TOF-PET. J Nucl Med. 2011;52:347–53 (* joint first authors).
91. Surti S, et al. Impact of time-of-flight PET on whole-body oncologic studies: a human observer lesion detection and localization study. J Nucl Med. 2011;52(5):712–9.
92. Daube-Witherspoon ME, et al. Determination of accuracy and precision of lesion uptake measurements in human subjects with time-of-flight PET. J Nucl Med. 2014;55:602–7.
93. Surti S. Update on time-of-flight PET imaging. J Nucl Med. 2015;56(1):98–105.
94. Buzhan P, et al. Silicon photomultiplier and its possible applications. Nucl Inst Methods Phys Res A. 2003;504(1–3):48–52.
95. Degenhardt C, et al. The digital Silicon Photomultiplier — A novel sensor for the detection of scintillation light. In: 2009 IEEE Nuclear Science Symposium Conference Record (NSS/MIC), Orlando; 2009.
96. Vandenberghe S, Marsden PK. PET-MRI: a review of challenges and solutions in the development of integrated multimodality imaging. Phys Med Biol. 2015;60:R115.
97. Miller M, et al. Initial characterization of a prototype digital photon counting PET system. Soc Nucl Med Ann Meet Abstr. 2014;55:658.
98. Levin C, et al. Initial results of simultaneous whole-body ToF PET/MR. Soc Nucl Med Ann Meet Abstr. 2014;55(Supplement 1):660P.
99. Schmand M, et al. BrainPET: first human tomograph for simultaneous (functional) PET and MR imaging. Soc Nucl Med Ann Meet Abstr. 2007;48(Supplement 2):45P.
100. Delso G, et al. Performance measurements of the Siemens mMR integrated whole-body PET/MR scanner. J Nucl Med. 2011;52(12):1914–22.
101. Freifelder R, et al. Design and performance of the head PENN-PET scanner. IEEE Trans Nucl Sci. 1994;41(4):1436–40.
102. Wienhard K, et al. The ECAT HRRT: performance and first clinical application of the new high resolution research tomograph. IEEE Trans Nucl Sci. 2002;49(1):104–10.
103. Watanabe M, et al. A new high-resolution PET scanner dedicated to brain research. IEEE Trans Nucl Sci. 2002;49(3):634–9.
104. Karp JS, et al. Performance of a brain PET camera based on anger-logic gadolinium oxyorthosilicate detectors. J Nucl Med. 2003;44(8):1340–9.
105. Surti S. Radionuclide methods and instrumentation for breast cancer detection and diagnosis. Semin Nucl Med. 2013;43:271–80.
106. Ishii K, et al. First achievement of less than 1 mm FWHM resolution in practical semiconductor animal PET scanner. Nucl Instrum Methods Phys Res, Sect A. 2007;576(2-3):435–40.
107. Drezet A, et al. CdZnTe detectors for small field of view positron emission tomographic imaging. Nucl Instrum Methods Phys Res, Sect A. 2007;571(1-2):465–70.
108. Mitchell GS, et al. CdTe strip detector characterization for high resolution small animal PET. IEEE Trans Nucl Sci. 2008;55(3):870–6.
109. Vaska P, et al. Ultra-high resolution PET: A CZT-based scanner for the mouse brain. J Nucl Med. 2009;50(2):293.